Journal of Sound and Vibration 377 (2016) 155–168

Contents lists available at ScienceDirect

Journal of Sound and Vibration

journal homepage: www.elsevier.com/locate/jsvi

Ray and wave scattering in smoothly curved thin shell cylindrical ridges

Niels Søndergaard [a], David J. Chappell [b,*]

[a] inuTech GmbH, Fürther Straße 212, 90429 Nuremberg, Germany
[b] School of Science and Technology, Nottingham Trent University, Nottingham NG11 8NS, United Kingdom

ARTICLE INFO

Article history:
Received 18 December 2015
Received in revised form
9 May 2016
Accepted 11 May 2016
Handling Editor: H. Ouyang
Available online 25 May 2016

Keywords:
Wave scattering
Ray tracing
Shell theory

ABSTRACT

We propose wave and ray approaches for modelling mid- and high-frequency structural vibrations through smoothed joints on thin shell cylindrical ridges. The models both emerge from a simplified classical shell theory setting. The ray model is analysed via an appropriate phase-plane analysis, from which the fixed points can be interpreted in terms of the reflection and transmission properties. The corresponding full wave scattering model is studied using the finite difference method to investigate the scattering properties of an incident plane wave. Through both models we uncover the scattering properties of smoothed joints in the interesting mid-frequency region close to the ring frequency, where there is a qualitative change in the dynamics from anisotropic to simple geodesic propagation.

1. Introduction

Thin shell components can be found in many large built-up mechanical structures such as cars, ships, and aeroplanes. The prediction of the mid- and high- frequency vibrational properties of these structures becomes computationally prohibitive for standard element-based methods, such as the finite element method [1]. The main reasons for this limitation are: firstly, very fine meshes are required for an adequate representation of the highly oscillatory wave solutions and the computational complexity grows with frequency raised to the power of the dimension of the space being modelled. Secondly, small uncertainties originating from the manufacturing process lead to a much larger variability in vibro-acoustic responses in the high frequency range [2], meaning that the response of any individual manufactured structure is of less interest to computer aided engineering practitioners than the average responses.

Methods such as statistical energy analysis (SEA) [2] and ray tracing [3] are more commonly applied for modelling wave problems at high frequencies. SEA has traditionally proved more popular for structural vibration problems with low damping [4], whereas ray tracing has found its niche in applications where relatively few reflections need to be tracked in computer graphics [3], room acoustics [5] and seismology [6]. Ray tracing has also been applied to elastic wave transmission problems on shells and plates [7]. In this context the ring frequency, that is the frequency above which longitudinal waves in a curved shell behave as they would in a flat plate, provides a useful point of reference. Beyond the ring frequency the ray dynamics in a curved shell are relatively simple following geodesic paths, but below the ring frequency one finds that asymptotic ray theories show richer features. The dispersion relations become highly anisotropic with likewise anisotropic

---

[*] Corresponding author.

http://dx.doi.org/10.1016/j.jsv.2016.05.019
0022-460X/

propagation [8]. An SEA treatment would fail to capture the non-trivial way in which the curved shell geometry influences the wave and ray propagation below the ring frequency [9], and hence ray methods can provide useful insight [7].

Wave scattering from discontinuous line joints below the ring frequency has been considered in [9,10]. However, manufacturers of large built-up mechanical structures are increasingly developing larger and lighter sub-components, whereby large thin shell structures are replacing more traditional plate-beam and multi-plate assemblies. The manufacturing process for such thin shells often entails casting molten metal (for example aluminium), which gives rise to curved components with smooth transitions between flat and curved regions. This raises the question of how the ray and wave scattering, and hence the vibrational properties of the structure, are modified in these smooth designs. In this work we study the case of a singly curved shell, chosen here as an assembly of two plates joined smoothly with a quarter of a cylinder. This simplified assembly represents a typical curved region within one of the larger sub-structures described above. We shall go beyond plane waves and ray tracing calculations by solving the full wave scattering problem numerically.

The numerical solution to the full wave scattering problem will be discussed in comparison with the corresponding ray tracing calculations. In both cases we find effective laws for the scattering properties, which may be inserted into ray or wave propagation modelling techniques such as dynamical energy analysis (DEA) [11,12] or the wave and finite element method [13,14]. In particular, combining these local scattering models within a larger model of a built-up structure will lead to a hybrid method for structures including curved thin shell components in the mid-frequency regime. Here, the natural definition of the mid-frequency regime is given by the range of frequencies that are high enough for a pure FEM analysis to be impractical, but low enough so that a simple geodesic description of the trajectory evolution is invalid. In the high-frequency case, DEA [11] can be applied to model the vibrational energy transport of a built-up structure along geodesic paths using the mesh data from a FEM analysis [12]. In fact, DEA presents a link between ray tracing and SEA by casting the wave or ray problem into the language of evolution operators. We note that an equivalent operator formalism has also been long known in computer graphics [15], although the theory underlying DEA arose from the more general setting of evolution operators for transporting flows in dynamical systems [16,17].

The organisation of the article is as follows: we introduce the necessary shell theory and derive a wave scattering model for a singly curved shell in Section 2. We then present two approaches for solving the wave scattering model; a short wavelength asymptotic ray tracing model based on this shell theory is detailed in Section 3, and a finite difference discretisation of the full wave model is described in Section 4. We then discuss and compare numerical results for both the wave and ray scattering models, and the resulting reflection and transmission laws in Section 5.

2. Thin shell wave theory

2.1. Governing equations of Donnell's shell theory

The thin shell theory of Donnell is one of the simplest and widely adopted models [7,18]. In this theory, moments and transverse forces are expressed by the displacement w of the middle surface as known from the theory of laterally loaded plates. As with other theories of continuum mechanics, shell theory is formulated in tensor form [19]. Some properties of tensors are summarised in Appendix A. We assume an isotropic shell of thickness h, Young's modulus E, density ρ and with Poisson ratio ν. The displacement vector of a point originally on the mid-surface of the shell is decomposed into tangential and normal components thus $\mathbf{u}=[u^1\ u^2\ w]^{\mathrm{T}}$.

The following tensor equation for the normal displacement w may be derived [7]

$$\rho h\frac{\partial^2 w}{\partial t^2} = -D_\alpha D_\beta\left(B(1-\nu)D^\alpha D^\beta w\right) - D_\alpha D^\alpha\left(B\nu D_\beta D^\beta w\right) - C((1-\nu)d^\alpha_\beta \epsilon^\beta_\alpha + \nu d^\alpha_\alpha \epsilon^\beta_\beta), \tag{1}$$

where

$$B=\frac{Eh^3}{12(1-\nu^2)} \quad \text{and} \quad C=\frac{Eh}{1-\nu^2} \tag{2}$$

are the bending and extensional stiffness, respectively. All Greek alphabet indices take values from the set $\{1,\ 2\}$. Also, the membrane strain is

$$\epsilon_{\alpha\beta} = \frac{1}{2}(D_\alpha u_\beta + D_\beta u_\alpha) + d_{\alpha\beta} w. \tag{3}$$

with $d_{\alpha\beta}$ the second fundamental form and D^α the covariant derivative. These are discussed further in the next section, where they are simplified for a singly curved shell. The tangential displacements $(u^1,\ u^2)$ in the directions (x^1, x^2), respectively, satisfy [7]

$$\rho h\frac{\partial^2 u^\alpha}{\partial t^2} = D_\beta\left(C\left((1-\nu)\epsilon^{\alpha\beta} + \nu\epsilon^\gamma_\gamma g^{\alpha\beta}\right)\right). \tag{4}$$

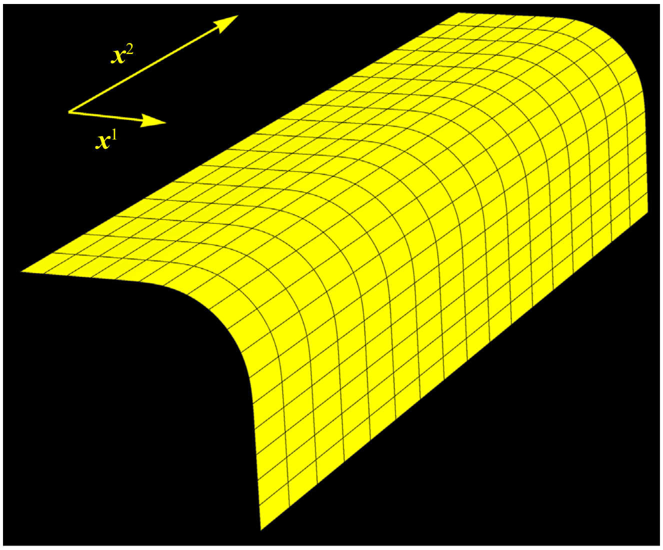

Fig. 1. The problem setting for which we derive a simplified set of shell equations: a cylindrical ridge connected to flat plates on either side.

The term $g^{\alpha\beta}$ represents the inverse of the first fundamental form as explained in Appendix A. Note that the above formulation is stated for a shell *in vacuo* and, although beyond the scope of the present study, coupling to an acoustic fluid may be included via an additional term in equation (1) to express the pressure difference on either side of the shell; see for example Ref. [7]. In addition, structural damping may be incorporated in the usual way by replacing the Young's modulus E in the equations above with $E(1+\mathrm{i}\eta)$, where η is the damping loss factor. However, we proceed with the lossless case $\eta=0$ in order to isolate the effect of curvature on the reflection and transmission properties of the shell, whilst also allowing us to check that our results conserve energy in the correct manner.

2.2. Simplified model for a singly curved shell

In this Section we simplify the shell theory presented above for thes case of a cylindrical ridge as shown in Fig. 1. The only simplifying assumption is that the shell is not curved with respect to the direction x^2. We define the principal curvature κ_1 (in the direction x^1) as

$$\kappa_1(x^1)=\frac{f(x^1)}{f(0)}\kappa_{\max}, \tag{5}$$

where $\kappa_{\max}$ is a constant corresponding to the maximum curvature in the cylindrical region. A smoothly varying curvature with respect to x^1 is obtained via the interpolation function f given by

$$f(x^1)=\frac{1}{2}\left(\operatorname{erf}\left(\frac{x^1+x^*}{\delta x}\right)-\operatorname{erf}\left(\frac{x^1-x^*}{\delta x}\right)\right), \tag{6}$$

where $x^1=\pm\, x^*$ are the centres of the transitions between the two flat regions where $\kappa_1=0$ and the cylindrical region where $\kappa_1=\kappa_{\max}$, see Fig. 2. Also, δx is the width of the transition region. Note that the case of a non-smooth joint between a cylindrical ridge and a pair of connecting plates is obtained in the limit $\delta x\to 0$.

A cylindrical ridge with a prescribed bending angle ψ can be designed by integrating the angular increment

$$\mathrm{d}\psi=\kappa_1\mathrm{d}x^1 \tag{7}$$

to find the total length L of the curved section of the geometry such that

$$\psi=\int_{-L/2}^{L/2}\kappa_1\mathrm{d}x^1 \tag{8}$$

for the desired angle. The length L is then found by numerically solving the implicit Eq. (8). In this work we take a quarter cylinder with $\psi=\pi/2$ as shown in Fig. 1.

In the above described geometrical setting, the shell theory presented in the last section is simplified considerably if we choose an orthonormal basis $(\mathbf{a}_1,\mathbf{a}_2)$ along the axes x^1,x^2. We then measure all tensor fields relative to this basis, that is, we work in physical components. The metric becomes

$$\mathrm{d}s^2=(\mathrm{d}x^1)^2+(\mathrm{d}x^2)^2 \tag{9}$$

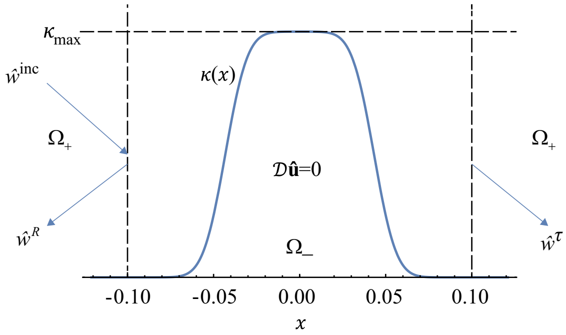

Fig. 2. The subdivision of the cylindrical ridge geometry into interior (Ω_-) and exterior (Ω_+) regions for the scattering problem. The interfaces between Ω_- and Ω_+ lie with the flat regions where $\kappa(x) \approx 0$. For $x \in \Omega_-$, the curvature increases smoothly to $\kappa(x) = \kappa_{\max}$ at $x=0$. The incident, reflected and transmitted waves in Ω_+ are also indicated.

and so the first fundamental form and its dual both reduce to the identity matrix

$$g_{\alpha\beta} := \mathbf{a}_\alpha \cdot \mathbf{a}_\beta = \delta_{\alpha\beta} = g^{\alpha\beta}. \tag{10}$$

Therefore the raising and lowering of indices becomes trivial. The second fundamental form $d_{\alpha\beta}$ in the basis $(\mathbf{a}_1, \mathbf{a}_2)$ is simply

$$d_{11} = \kappa_1, \tag{11}$$

and zero for all other combinations of α and β.

The covariant derivative (see Appendix A), likewise reduces considerably since all derivatives vanish for the metric Eq. (10). Hence, all Christoffel symbols vanish and the covariant derivative is identical to the directional derivative, i.e. $D_\alpha = \partial_\alpha$. Applying the above simplifications in the shell equation for the normal displacement (1) and assuming that material constants and the thickness are constant yields the following equation

$$\rho h \frac{\partial^2 w}{\partial t^2} = -B\Delta^2 w - C\kappa\left(\frac{\partial u^1}{\partial x} + \nu \frac{\partial u^2}{\partial y} + \kappa w\right), \tag{12}$$

where we write $(x^1, x^2) \equiv (x, y)$ and $\kappa_1(x^1) \equiv \kappa(x)$ for simplicity of notation. We adopt this notation for the remainder of the paper since we are no longer considering differential equations written in tensor form. Repeating the simplification process for the in-plane wave equation system (4) gives

$$\frac{\rho h}{C}\frac{\partial^2 u^1}{\partial t^2} = \frac{\partial^2 u^1}{\partial x^2} + \frac{(1+\nu)}{2}\frac{\partial^2 u^2}{\partial x \partial y} + \frac{(1-\nu)}{2}\frac{\partial^2 u^1}{\partial y^2} + \frac{\partial}{\partial x}(\kappa w), \tag{13}$$

$$\frac{\rho h}{C}\frac{\partial^2 u^2}{\partial t^2} = \frac{\partial^2 u^2}{\partial y^2} + \frac{(1+\nu)}{2}\frac{\partial^2 u^1}{\partial x \partial y} + \frac{(1-\nu)}{2}\frac{\partial^2 u^2}{\partial x^2} + \nu\kappa\frac{\partial w}{\partial y}. \tag{14}$$

Hence, a simplified set of partial differential equations (PDEs) describe the wave motion in the cylindrical ridge shell geometry under consideration here. In the next section we discuss how under certain modelling assumptions, this system can be reduced further to a set of ordinary differential equations (ODEs).

2.3. Reduction to a system of ordinary differential equations

In this work we are primarily interested in how the scattering properties of a thin shell cylindrical ridge depend on the frequency and the direction of a prescribed incident plane wave originating in the flat region (where $\kappa \sim 0$). As such it makes sense to consider time-harmonic waves with angular frequency ω. Further, we can extract scattering properties that are independent of the position along the ridge by exploiting the translational symmetry and assuming that the ridge is of infinite extent in the $y-$ direction. Under these assumptions we may write

$$\mathbf{u}(x, y, t) = \hat{\mathbf{u}}(x) e^{\mathrm{i}(k_y y - \omega t)}, \tag{15}$$

where k_y is the component of the wavenumber in the $y-$ direction and $\hat{\mathbf{u}} = [u \ v \ \hat{w}]^{\mathrm{T}}$ are the coefficients of (15) in the in-plane directions x and y, and the normal direction, respectively. Substitution of the ansatz (15) into the PDE system (12)–(14) yields the following fourth-order ODE system in the variable x:

$$c_p^2 \frac{\mathrm{d}^2 u}{\mathrm{d}x^2} + \left(\omega^2 - c_s^2 k_y^2\right) u + \mathrm{i}k_y \left(c_p^2 - c_s^2\right)\frac{\mathrm{d}v}{\mathrm{d}x} + c_p^2 \frac{\mathrm{d}}{\mathrm{d}x}(\kappa \hat{w}) = 0, \tag{16}$$

$$c_s^2 \frac{\mathrm{d}^2 v}{\mathrm{d}x^2} + \left(\omega^2 - c_p^2 k_y^2\right) v + \mathrm{i}k_y \left(\left(c_p^2 - c_s^2\right)\frac{\mathrm{d}u}{\mathrm{d}x} + \nu c_p^2 \kappa \hat{w}\right) = 0, \tag{17}$$

$$\frac{B}{\rho h}\left(\frac{\mathrm{d}^4\hat{w}}{\mathrm{d}x^4}-2k_y^2\frac{\mathrm{d}^2\hat{w}}{\mathrm{d}x^2}+k_y^4\hat{w}\right)+\left(c_p^2\kappa^2-\omega^2\right)\hat{w}+c_p^2\kappa\left(\frac{\mathrm{d}u}{\mathrm{d}x}+i\nu k_y v\right)=0. \tag{18}$$

Note that the constants in the above system have been simplified by writing them in terms of the pressure and shear wave velocities,

$$c_p=\sqrt{\frac{E}{\rho(1-\nu^2)}} \quad \text{and} \quad c_s=\sqrt{\frac{E}{2\rho(1+\nu)}},$$

respectively. In particular, we have made use of the following easily verified relations

$$c_p^2=\frac{C}{\rho h}, \quad \frac{c_s^2}{c_p^2}=\frac{(1-\nu)}{2} \quad \text{and} \quad c_p^2-c_s^2=\frac{(1+\nu)c_p^2}{2}.$$

Later in the paper we will write the above ODE system in the shorthand form

$$\mathcal{D}\hat{\mathbf{u}}=0, \tag{19}$$

for brevity of exposition.

2.4. Formulation of the scattering problem

We connect the curved region to flat plates on each side using interfaces. Imposing a set of conditions at these interfaces will enable us to formulate the set of ODEs (19) as a boundary value problem, and then by considering the flux of the incoming and outgoing wave fields at these interfaces we are able to formulate a scattering problem. We assume that the interfaces reside in the asymptotically flat regions and as such the interfaces themselves do not give rise to reflection/transmission phenomena, only the interior region between the interfaces governs the scattering properties.

Each interface is assumed to satisfy the continuity conditions given in Ref. [10], that is, continuity of displacement, rotation, traction, moment, and normal shear stress. Since the material properties are constant throughout the entire geometry, then the interface conditions may be written simply as

$$\hat{\mathbf{u}}^-=\hat{\mathbf{u}}^+, \tag{20}$$

$$\frac{\mathrm{d}\hat{\mathbf{u}}}{\mathrm{d}x}^-=\frac{\mathrm{d}\hat{\mathbf{u}}}{\mathrm{d}x}^+, \tag{21}$$

$$\frac{\mathrm{d}^2\hat{w}}{\mathrm{d}x^2}^-=\frac{\mathrm{d}^2\hat{w}}{\mathrm{d}x^2}^+, \tag{22}$$

$$\frac{\mathrm{d}^3\hat{w}}{\mathrm{d}x^3}^-=\frac{\mathrm{d}^3\hat{w}}{\mathrm{d}x^3}^+. \tag{23}$$

The superscripts specify the value of the quantity as we approach the interface from either the interior region (−) containing the ridge, or the exterior flat region (+) beyond the interfaces on either side of the ridge. In the sequel we will refer to the interior region as Ω_-, and the union of the exterior regions as Ω_+ (see Fig. 2).

The waves in Ω_+ are precisely those of classical plate theory and therefore the wave modes in Ω_+ that are scattered by Ω_- will be one (or more) of bending, pressure, shear or evanescent bending type. In relation to the vector $\hat{\mathbf{u}}$ we have that $\hat{w}$ describes the sum of the bending wave contributions and that the in-plane wave types will each be given by a linear combination of u and v. In this work we consider only incident bending modes $\hat{w}^{\mathrm{inc}}$ originating in the exterior Ω_+ and being scattered by the ridge in Ω_-. However, the extension to other incident wave types is straightforward. For the purpose of investigating directional properties we consider plane wave scattering. We introduce the notation that the interface to the left of Ω_- is located at $x=x^l$ and the interface to the right is correspondingly at $x=x^r$. Then an incident wave of unit amplitude travelling in from the left of Ω_- can be written in the form

$$\hat{w}^{\mathrm{inc}}(x)=\exp(\mathrm{i}k_x^b(x-x^l)), \tag{24}$$

where k_x^b is the wave-number associated with the incident bending mode in the x-direction. In order to write the resulting scattered waves in a concise manner we introduce $x_\tau=x-x^r$ and $x_R=x-x^l$. Then the scattered waves in Ω_+ may be written

$$\varphi_\beta^\alpha(x)=A_\beta^\alpha\exp(\pm\mathrm{i}k_x^\alpha x_\beta), \tag{25}$$

where $\alpha\in\{b,e,p,s\}$ designates the scattered wave type as either bending (b), evanescent bending (e), pressure (p) or shear (s). The symbol $\beta\in\{R,\tau\}$ designates whether the scattered wave is reflected (R) or transmitted (τ). That is, whether the scattered wave emerges in Ω_+ on the same side of the ridge as the incident wave is sent in, or on the other side. The value of β also prescribes the sign in the $\pm$ as negative for $\beta=R$ and positive for $\beta=\tau$. The coefficient A_β^α denotes the corresponding wave amplitude, which are related to $\hat{\mathbf{u}}$ via the following relations

$$u^{\beta}(x) = \pm A^{p}_{\beta}\exp(\pm \mathrm{i}k^{p}_{x}x_{\beta})\cos\theta - A^{s}_{\beta}\exp(\pm \mathrm{i}k^{s}_{x}x_{\beta})\sin\theta, \tag{26}$$

$$v^{\beta}(x) = A^{p}_{\beta}\exp(\pm \mathrm{i}k^{p}_{x}x_{\beta})\sin\theta \pm A^{s}_{\beta}\exp(\pm \mathrm{i}k^{s}_{x}x_{\beta})\cos\theta, \tag{27}$$

$$\hat{w}^{\beta}(x) = A^{b}_{\beta}\exp(\pm \mathrm{i}k^{b}_{x}x_{\beta}) + A^{e}_{\beta}\exp(-k^{b}_{x}|x_{\beta}|). \tag{28}$$

Here $\theta \in (-\pi/2, \pi/2)$ is the angle between the scattered wave directions and the $x-$ axis (positive or negatively oriented depending on the direction of propagation). Hence, the total wave field in Ω_+ to the left of Ω_- is given by

$$\hat{\mathbf{u}}^{l} = [u^{R}\ \ v^{R}\ \ \hat{w}^{R} + \hat{w}^{\mathrm{inc}}]^{\mathrm{T}}, \tag{29}$$

and the total wave field to the right of Ω_- may be written

$$\hat{\mathbf{u}}^{r} = [u^{\tau}\ \ v^{\tau}\ \ \hat{w}^{\tau}]^{\mathrm{T}}. \tag{30}$$

The scattering problem is then formed by connecting the interior problem for $\hat{\mathbf{u}} = \hat{\mathbf{u}}^{-}$ in Ω_- with the plane wave ansatz in the exterior regions for $\hat{\mathbf{u}}^{l}$ and $\hat{\mathbf{u}}^{r}$ described above, via the interface conditions (20) to (23). Here $\hat{\mathbf{u}}^{l}$ and $\hat{\mathbf{u}}^{r}$ take the role of $\hat{\mathbf{u}}^{+}$ on the left and right interfaces, respectively. When this scattering problem is solved, we can extract the scattering solutions $\hat{\mathbf{u}}^{l}$ and $\hat{\mathbf{u}}^{r}$ and the scattering coefficients A^{α}_{β}, the latter of which are of primary interest for this study.

3. From waves to rays: short wavelength asymptotics

One obtains a ray tracing model from the PDE model (12) – (14) by moving to short wavelength asymptotics using the ansatz

$$\mathbf{u}(x, y, t) = \mathbf{u}^{(\varepsilon)}(x, y, t)\exp\left(\mathrm{i}\varepsilon^{-\lambda}\phi(x, y, \varepsilon^{\mu}t)\right),$$

where ϕ is a phase function and ε is a small parameter. The choice of the parameters $\lambda \geq 0$ and $0 \leq \mu \leq \lambda$ determines the wave type, bending or in-plane. Then we define the frequency $\omega = -\partial_t\phi(x, y, \varepsilon^{\mu}t)$ and the wavenumber vector $\mathbf{k} = \nabla\phi$. Note that the pre-factors of t vanish after applying the asymptotic scaling and setting $\lambda = \mu = 0$. Assuming that $k = |\mathbf{k}|$ is large in comparison to the curvature, Pierce derived a general dispersion relation [18] that was later presented in a simpler form by Norris and Rebinsky [7]. In the next section we apply this dispersion relation to generate the Hamiltonian dynamics for our ray tracing model on a singly curved shell.

3.1. Below the ring frequency

The ring frequency for the cylinder is defined relative to the pressure mode and corresponds to the frequency above which a longitudinal wave can traverse around the cylinder. This extensional motion gives rise to radial motion, which also results in breathing modes in cylinders. In the vicinity of the ring frequency, approximate forms of the dispersion relations are obtained for the in-plane and bending modes using different scalings. These dispersion relations each reduce to those for a flat plate when the frequency sufficiently exceeds the ring frequency. Hence in this study, we refer to the mid-frequency case as the the frequency range in the vicinity of the ring frequency and the high frequency regime as the frequencies that are sufficiently large for the dispersion relations to reduce to those of a flat plate. Defining the longitudinal wavenumber to be $\Omega = \omega/c_p$, with c_p the longitudinal plate wave speed as before, and denoting the corresponding wavenumber at the ring frequency as Ω_*, we find that $\Omega_* = \kappa$ for the singly curved shell configuration shown in Fig. 1.

Below the ring frequency, the full dispersion relationship is usually considered. For the configuration in Fig. 1 with zero curvature in the $y-$ direction we obtain the following expression from Ref. [7] in physical coordinates:

$$\tilde{H}(x, k, \omega) = \left(\Omega^2 - \frac{1}{2}k^2(1-\nu)\right)\left(\left(\Omega^2 - k^2\right)\left(\Omega^2 - \frac{h^2k^4}{12}\right) - \Omega^2\Omega_*^2\right) \tag{31}$$

$$+ (1-\nu^2)\left(\Omega^2\kappa^2k_y^2 - \frac{1}{2}(1-\nu)\kappa^2k_y^4\right).$$

Two extreme cases of the dispersion curve are depicted in Fig. 3, which shows the respective dispersion relations for a cylinder and for a flat plate using the parameters given in Appendix B. The outer part of the cylinder dispersion curve has also been observed experimentally [8].

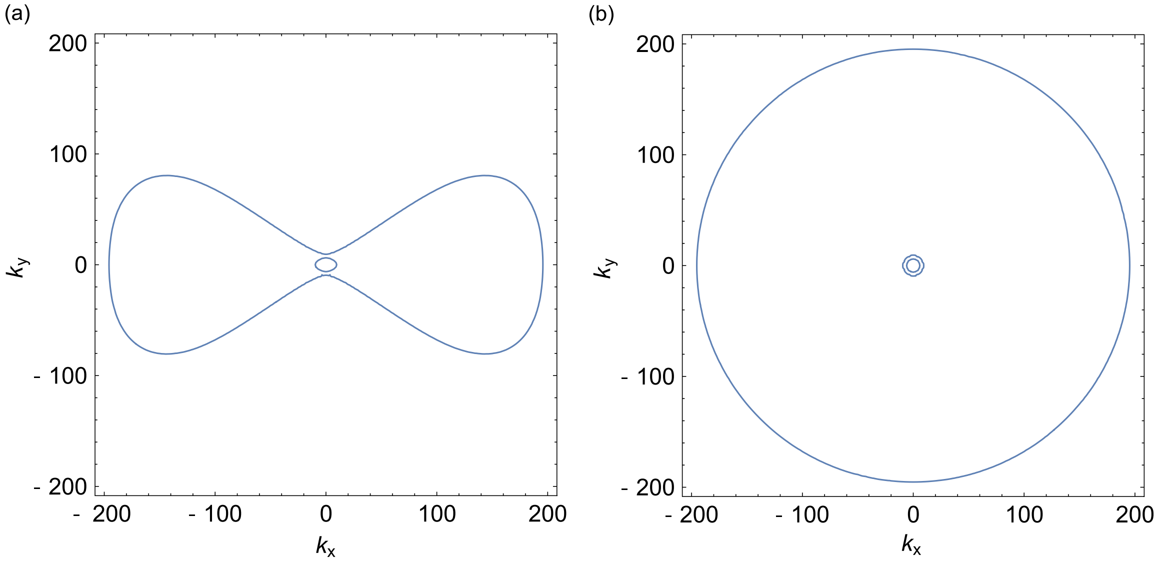

Fig. 3. Dispersion relations represented by plotting $\Omega(k_x, k_y)$ at zeros of the Hamiltonian $\tilde{H}$. (a) Anisotropic dispersion relation for a cylinder. (b) Isotropic dispersion relation for a flat plate.

3.2. Hamiltonian system

The Hamiltonian $\tilde{H}$ (31) gives rise to the following ODE system, which governs the ray dynamics on a singly curved shell

$$\dot{x} = \frac{\partial \tilde{H}}{\partial k_x}, \tag{32}$$

$$\dot{y} = \frac{\partial \tilde{H}}{\partial k_y}, \tag{33}$$

$$\dot{k}_x = -\frac{\partial \tilde{H}}{\partial x}, \tag{34}$$

$$\dot{k}_y = -\frac{\partial \tilde{H}}{\partial y}. \tag{35}$$

In a full time-domain simulation one would also have two additional equations

$$\dot{t} = -\frac{\partial \tilde{H}}{\partial \omega}, \tag{36}$$

$$\dot{\omega} = \frac{\partial \tilde{H}}{\partial t}. \tag{37}$$

In this work however, the frequency is constant due to the fact our Hamiltonian $\tilde{H}$ is time-independent. Furthermore, since we also take the material parameters to be constants throughout the shell, equation (36) simply represents a re-parametrisation of time to the fictitious time used here. Eqs. (36) and (37) are therefore not needed in the time-harmonic description. Finally, due to the translational invariance in the y-direction, k_y is constant and it suffices to study the above Hamiltonian system in the (x, k_x) phase-plane only.

4. Discretisation of the wave scattering problem

In order to solve the full wave scattering problem we discretise the ODE system in Ω_- using finite difference methods and couple this to the scattering of incoming and outgoing waves in Ω_+ using the interface coupling conditions as described below.

4.1. Finite difference method in Ω_-

The differential operator $\mathcal{D}$ in the ODE system (19) includes both bending and in-plane waves, along with the coupling between them. Each of the equations in the system is discretised using second order accurate centered finite difference (FD) formulae on a set of equi-spaced grid points $\{x_j\}$ with $j = 0, \ldots, N$. We denote the centered finite difference matrices for approximating derivatives of order n by $\mathbf{D}_0^n$ and define

$$\boldsymbol{\kappa} = [\kappa(x_i)\delta_{ij}] \quad \text{with} \quad i,j = 0, \ldots, N, \tag{38}$$

to be a diagonal matrix containing the curvature values.

To create a vectorial ODE discretisation we use the Kronecker product $\otimes$, see for example Ref. [20], along with the following 3×3 projector matrices:

$$\mathbf{E}_{ij} = [\delta_{ia}\delta_{jb}] \text{ for } a, b = 1, 2, 3, \tag{39}$$

$$\Pi_i = \mathbf{E}_{ii}, \tag{40}$$

$$\mathbf{H}_{23} = \begin{bmatrix} 0 & 0 & 0 \\ 0 & 0 & \mathrm{i} \\ 0 & -\mathrm{i} & 0 \end{bmatrix}. \tag{41}$$

Using the above notation we can write the various operators of our ODE in a compact way. The in-plane Eqs. (16) and (17) will have a diagonal (self-interaction) and frequency independent part

$$\mathbf{M}_{\text{diag}} = (c_p^2 \mathbf{D}_0^2 - c_s^2 k_y^2 \mathbf{I}) \otimes \Pi_1 + (c_s^2 \mathbf{D}_0^2 - c_p^2 k_y^2 \mathbf{I}) \otimes \Pi_2, \tag{42}$$

where $\mathbf{I}$ is the 3×3 identity matrix. The coupling between the u and v components is symmetric and is given by

$$\mathbf{M}_{\text{off}} = \mathrm{i}k_y(c_p^2 - c_s^2)\mathbf{D}_0^1 \otimes (\mathbf{E}_{12} + \mathbf{E}_{21}). \tag{43}$$

The bending wave Eq. (18) has a diagonal (self-interaction) and frequency independent part

$$\mathbf{B} = -\left(\frac{B}{\rho h}\left(\mathbf{D}_0^4 - 2k_y^2\mathbf{D}_0^2 + k_y^4\mathbf{I}\right) + c_p^2\boldsymbol{\kappa}^2\right) \otimes \Pi_3, \tag{44}$$

and the coupling between the bending and in-plane components is given by

$$\mathbf{C} = c_p^2(\mathbf{D}_0^1\boldsymbol{\kappa} \otimes \mathbf{E}_{13} - \boldsymbol{\kappa}\mathbf{D}_0^1 \otimes \mathbf{E}_{31} + k_y\nu\boldsymbol{\kappa} \otimes \mathbf{H}_{23}). \tag{45}$$

The shell operator $\mathcal{D}$ then has the following discrete representation:

$$\mathbf{D} = \mathbf{M}_{\text{diag}} + \mathbf{M}_{\text{off}} + \mathbf{B} + \mathbf{C} + \omega^2\mathbf{I}. \tag{46}$$

The FD operators will extend beyond the grid over Ω_- as the stencil reaches into the scattering region. This leads to a coupling between the degrees of freedom in the finite difference approximation and the unknown scattering amplitudes A_β^α. Conversely, the incident wave in Ω_+ will produce a forcing term which drives the finite difference calculation in Ω_-. This coupling of the FD solution in Ω_- and the plane wave description in Ω_+ is discussed further below.

4.2. Coupling of the interior and exterior regions

The scattering solution and its derivatives in Ω_+ are matched to the FD solution in Ω_- at the interfaces between Ω_- and Ω_+ according to the conditions (20) to (23). The incident wave gives rise to inhomogeneous terms for the excitation of the FD model at the left interface. The derivatives appearing in the coupling conditions are implemented in the FD-solution in Ω_- using one-sided finite difference operators with second order accuracy. Forward difference formulae are employed at the left interface and backward difference formulae are employed at the right interface so that the stencils extend only into Ω_-. The extremal points of these stencils are taken at the scattering boundaries, where the value of the scattering solution is applied as a boundary condition. The interfaces are thus taken to be at positions Δx away from the extremal inner grid points, where Δx is the discretisation step in the FD approximation.

As an illustrative example we consider the condition on $\mathrm{d}^3\hat{w}/\mathrm{d}x^3$ (23) at the interface receiving the incident wave (24). The reflected bending modes include both a propagative contribution $A_R^b \exp\left(-\mathrm{i}k_x^b x_R\right)$ and an evanescent contribution $A_R^e \exp\left(-k_x^b|x_R|\right)$ as shown in equation (28). The forward difference formula for the third derivative takes the form

$$V(f) := D_+^3 f_0 = \frac{1}{\Delta x^3}\left(-\frac{5}{2}f_0 + 9f_1 - 12f_2 + 7f_3 - \frac{3}{2}f_4\right). \tag{47}$$

Matching the scattering and finite difference solutions using the interface condition (23) leads to

$$\frac{\mathrm{d}^3}{\mathrm{d}x^3}\left(\hat{w}^{\text{inc}} + A_R^b \exp\left(-\mathrm{i}k_x^b x_R\right) + A_R^e \exp\left(-k_x^b|x_R|\right)\right) = V(\hat{w}). \tag{48}$$

Splitting the discretised boundary operator V into a part that acts only on the left-most entry at the interface and one that acts on the remaining nodes in Ω_-, we obtain

$$V=\delta_{\mathrm{i}0}V+(1-\delta_{\mathrm{i}0})V:=V_0+\overline{V},\quad i=0,\ldots,4. \tag{49}$$

At $x=x_l=x_0$, the left hand side of (48) evaluates to

$$-(k_x^b)^3(\mathrm{i}+\mathrm{i}A_R^b+A_R^e), \tag{50}$$

and using the splitting described above, the right hand side may be written as

$$V_0\left(1+A_R^b+A_R^e\right)+\overline{V}(\hat{w}). \tag{51}$$

Writing $\hat{w}_i\approx\hat{w}(x_i)$ for $i=1,2,3,4$ and using the definition of V yields a linear equation

$$(k_x^b)^3\left(\mathrm{i}+\mathrm{i}A_R^b+A_R^e\right)=\frac{5(1+A_R^b+A_R^e)-18\hat{w}_1+24\hat{w}_2-14\hat{w}_3+3\hat{w}_4}{2\Delta x^3} \tag{52}$$

in terms of the unknowns A_R^b, A_R^e and $\hat{w}_i$, $i=1,2,3,4$. Continuing for the remaining boundary conditions at the left interface $x=x_0$ yields similar relations, all following the same pattern as in (52). The boundary conditions at the right interface give similar results for the transmitted terms, but without the incident wave terms. Finally, we combine the discretised interface coupling conditions with the interior finite difference equations. This leads to the matrix problem:

$$\begin{bmatrix} * & * & \mathbf{0} \\ * & \mathbf{D} & * \\ \mathbf{0} & * & * \end{bmatrix}\begin{bmatrix} \mathbf{R} \\ \hat{\mathbf{u}}_\Delta \\ \mathbf{T} \end{bmatrix}=\begin{bmatrix} * \\ \mathbf{0} \\ \mathbf{0} \end{bmatrix} \tag{53}$$

with scattering coefficients

$$\mathbf{R}=[A_R^b\ A_R^e\ A_R^p\ A_R^s]^\mathrm{T}, \tag{54}$$

and

$$\mathbf{T}=[A_\tau^b\ A_\tau^e\ A_\tau^p\ A_\tau^s]^\mathrm{T}. \tag{55}$$

Here, the finite difference solution in the interior of Ω_- is represented by

$$\hat{\mathbf{u}}_\Delta=\left[u_i\ v_i\ \hat{w}_i\right]^\mathrm{T},\ i=1,\ldots,N-1. \tag{56}$$

Note that the stencil for the second derivative FD operator within **D** takes boundary data from the plane wave terms at the interface points x_0 and x_N, whereas the fourth derivative operator extends beyond this and also takes boundary data from within the scattering region at $x=x_0-\Delta x$ and $x=x_N+\Delta x$.

5. Numerical results

In this section we discuss the numerical solution of the full wave scattering problem derived in Section 2 and compare the results to those obtained using an ODE time-stepper for the Hamiltonian system presented in Section 3. The parameters chosen for all calculations are summarised in Appendix B. For the cylindrical region, these parameters correspond to a circularly cylindrical steel shell as considered in Refs. [8,21]. Note that whilst the width of the cylindrical ridge studied here is on the millimeter scale, it only represents a small region of the larger structures and components that serve to motivate this study.

An incident bending mode in the left part of Ω_+ is used to excite the system and is sent in to the interface with Ω_- at various angles, corresponding to a variation in the trace wave number k_y^b. The latter is chosen according to the values given by the dispersion curve. In all cases we set $\omega=9742\pi$ Rad/s, which is large enough so that waves will always transmit straight through the cylindrical region (as though it were a flat plate) when $k_y^b=0$, that is when waves approach the cylindrical region directed parallel to the x-axis. We note that in the high frequency regime this behaviour will be preserved for almost all incident waves when both k_x^b and k_y^b are positive. However, the choice of ω here corresponds to the more interesting mid-frequency case where reflections are also possible for a range of sufficiently large $k_y^b>0$.

5.1. Ray tracing calculations

In this section we consider the reflection/ transmission behaviour of rays corresponding to an incident bending mode (see Fig. 4). A range of incoming wavenumbers (directions) are used corresponding to the strip in the upper left corner of the figure. We find that the rays transmit for sufficiently large k_x^b, whereas for smaller positive values of k_x^b the rays reflect. Note that the symmetry of the problem means that rays also transmit for k_x^b negative when the incoming ray is from the right hand side and $|k_x^b|$ is large enough. The threshold value of (k_x^b,k_y^b) for the change from reflectance to transmittance corresponds to a hyperbolic fixed point and its location can be found conveniently by considering the sizes of the dispersion curves as discussed in [22]. The upper fixed point shown in both parts of Fig. 4 gives a threshold value of

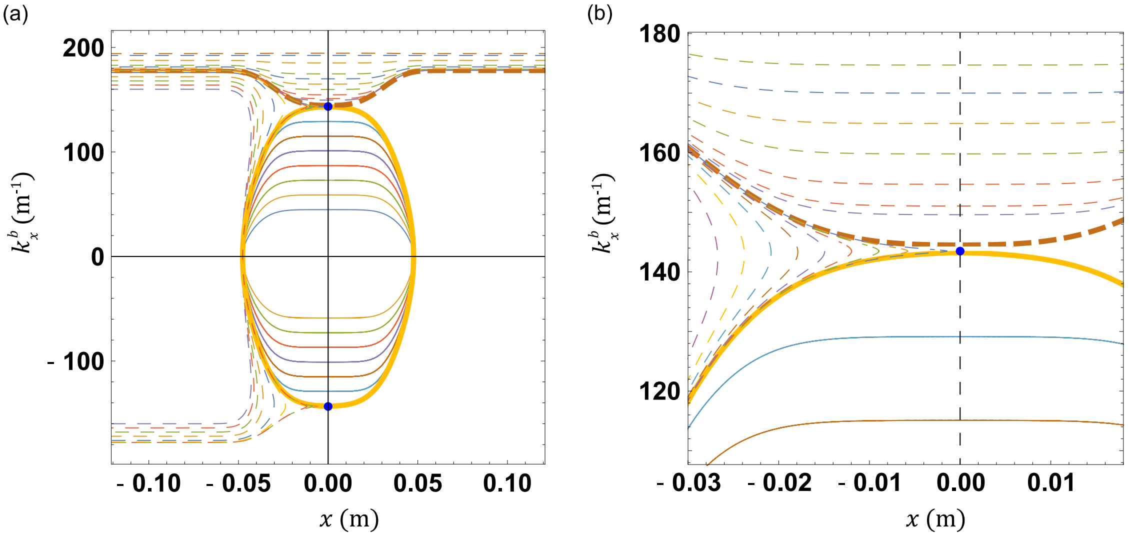

Fig. 4. (a) Ray trajectories represented in the (x, k_x^b) phase-plane showing two fixed points at $x=0$ and the separatrix (solid bold curve) which connects them as it traverses the cylindrical ridge. (b) A close up view of the upper fixed point and separatrix region. The upper fixed point divides the incoming rays from the left hand side (dashed lines) into reflecting or transmitting trajectories. The bold dashed line depicts the extremal transmitting trajectory closest to the set of reflecting rays. In both subplots, the solid line trajectories are those which are trapped inside the ridge.

$(k_x^b, k_y^b) = (143\mathrm{m}^{-1}, 80.5\mathrm{m}^{-1})$. We will also investigate the existence and location of such a threshold incoming wave direction in the finite difference solution of the full wave problem described in the next section.

Depending on the angle of incidence, Fig. 4 shows that the point of reflection varies from the centre of the ridge at $x=0$ to slightly towards the flat region to the left. The smooth curvature model here therefore differs from the discontinuous curvature models considered in Refs. [9,10], for which the reflection takes place off-centre at a fixed location only. That is, for the models presented in Refs. [9,10] the reflection would take place at the location of the jump in the curvature between the flat region and the cylindrical region. This would be off-centre in the example here, since the centre point $x=0$ corresponds to the centre of the cylindrical region.

In the next section we consider an equivalent scattering problem to the one above, but instead using the finite difference model described in the previous section to numerically solve the full wave problem. The full wave model will include the phase information omitted in the pure ray approximation applied in this section, but at the cost of a computational expense which scales with frequency. Such a study is feasible up to reasonably high frequencies due to the one-dimensional setup of the problem derived in Section 2. However, the high frequency purely transmissive behaviour for the problem here is relatively straightforward to predict, and we find that both methods may be used for the more interesting mid-frequency case studied here.

5.2. *Wave scattering finite difference solution*

We restrict the study to bending excitations as in the previous section. For smooth joints this means that only the bending mode is active, with negligible conversion to in-plane modes. That is, the scattering probabilities become

$$P(\text{Transmit}) = |A_\tau^b|^2 \quad \text{and} \quad P(\text{Reflect}) = |A_R^b|^2 \tag{57}$$

using the scattering amplitudes for bending only. However, for rapidly changing curvature functions (5) with very small δx in the interpolation function (6), mode conversions appeared in the numerics at almost normal incidence. We defer the study of this case to future work and note the possibility of using discontinuous joints instead for this case. Note that we use the term probabilities to describe the coefficients defined in (57) since for an incoming bending wave of unit amplitude (24), conservation of energy gives that $P(\text{Transmit}) + P(\text{Reflect}) = 1$. In the full wave picture considered here these coefficients (57) actually give the proportions of reflected and transmitted wave energy. However, for comparison with the ray tracing results in the last section, they give the probabilities of reflection and transmission for a particular incoming trajectory.

The dependence of the reflection and transmission probabilities on the value of the trace wave number k_y^b is shown in Fig. 5. The transmission and reflection probabilities have been computed using the finite difference discretisation described in Section 4 for both $N=500$ and $N=1000$ grid points in Ω_-, corresponding to $\Delta x = 0.0048384$ m and $\Delta x = 0.0024192$ m, respectively. The ratio of wavelength to Δx is 6.65 for the case $N=500$ and hence the rule of thumb requiring 6 points per wavelength for reliable results suggests that in both cases our results should be reasonably well converged. This convergence is also evident from Fig. 5, since it is difficult to detect differences between the plots for $N=500$ and $N=1000$.

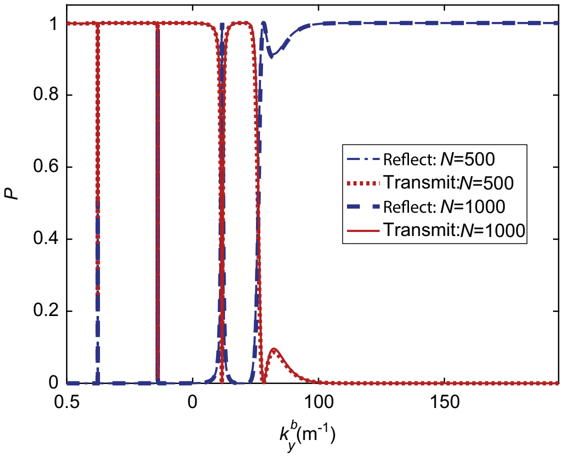

Fig. 5. Reflection and transmission probabilities for the bending mode as a function of k_y^b plotted on a linear scale. The plot shows anti-resonances close to $k_y^b = 12.3\text{m}^{-1}$, $k_y^b = 36.2\text{m}^{-1}$ and $k_y^b = 61.7\text{m}^{-1}$. There is a switch in the dominant behaviour from transmission to reflection close to $k_y^b = 78\text{m}^{-1}$.

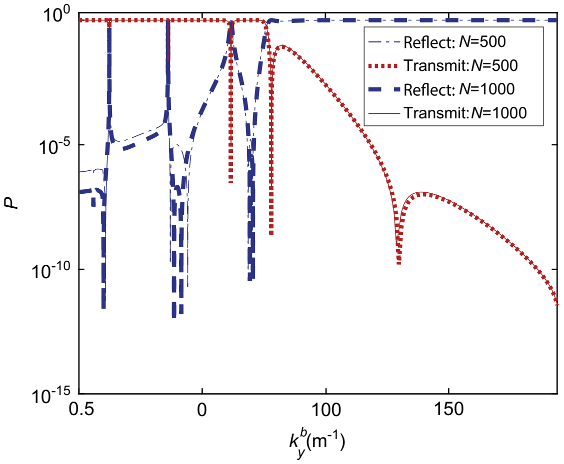

Fig. 6. Reflection and transmission probabilities for the bending mode as a function of k_y^b plotted on a logarithmic scale. The logarithmic scale emphasises the anti-resonance reflection peaks and the switch from transmission to reflection that were evident from Fig. 5.

Fig. 5 shows that the scattering coefficients of the full wave problem include discrete anti-resonance points (points of perfect reflection) that were not present in the ray tracing calculation. In addition, the threshold behaviour from transmission to reflection has been smoothed in the full wave calculations, whereas for the ray tracing solution there is a sudden jump from transmission to reflection corresponding to the location of the hyperbolic fixed point. Hence, for the calculations in this section there is a region of k_y^b values where both reflection and transmission take place at the same time. This region lies roughly between $k_y^b = 73\text{m}^{-1}$ and $k_y^b = 95\text{m}^{-1}$, but one observes an obvious switch from dominant transmission behaviour to dominant reflection behaviour at a threshold value around $k_y^b = 78\text{m}^{-1}$, which is close to the threshold estimate ($k_y^b = 80.5\text{m}^{-1}$) from the corresponding ray tracing calculation. It appears therefore that the asymptotic ray model slightly over predicts the transmission/reflection threshold compared with the full wave solution, but still produces a reliable estimate within around 1% of the total k_y^b range.

A more complete picture appears when the scattering coefficients are plotted on a logarithmic scale, see Fig. 6. We can then clearly identify the discrete reflection points in the region of perfect transmission. The dips or peaks can be arbitrarily close to zero, or unity, depending on the resolution of the plot. The discrepancy between the finite difference solution for the reflection coefficient with $N = 500$ and $N = 1000$ is also more evident in this figure since the logarithmic scaling amplifies the differences at very small values of $P(\text{Reflect})$ below 10^{-4}. However, the positions of the anti-resonances and the switch from transmission to reflection remain in excellent agreement for both $N = 500$ and $N = 1000$. Note also that the values of $P(\text{transmit})$ computed with $N = 500$ and $N = 1000$ are in good agreement with one another, even for very small values.

Fig. 7 shows the behaviour of the wave function solutions $\hat{\mathbf{u}} = [u\ v\ \hat{w}]^{\mathrm{T}}$ for various values of the trace wavenumber k_y^b. The finite difference computations for these plots were all carried out using $N = 1000$ grid points. Note that there is no mode conversion and so the in-plane contributions u and v only have support on the curved region and vanish in Ω_+. In the case

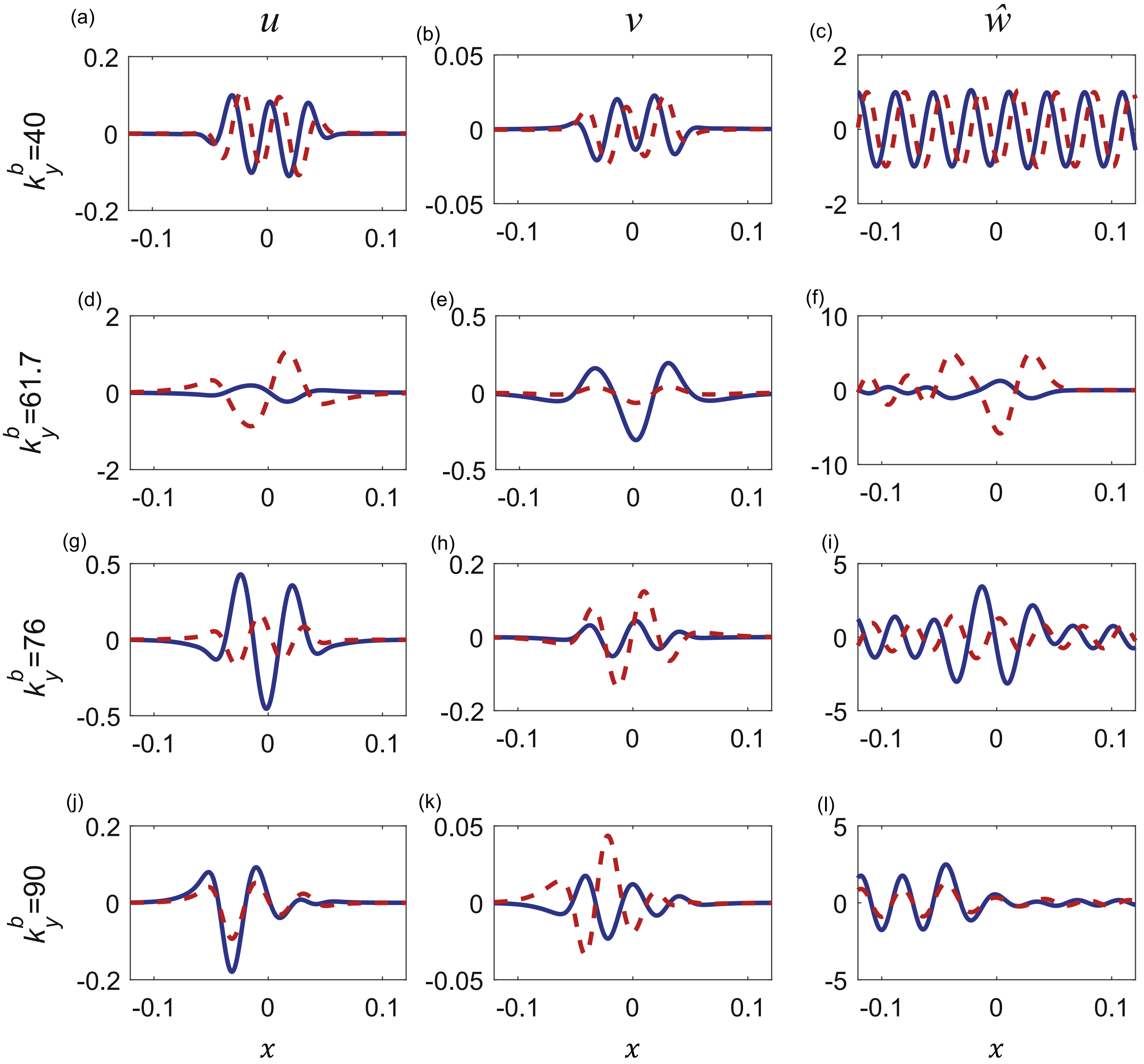

Fig. 7. Wave function solutions $\hat{\mathbf{u}} = [u\ v\ \hat{w}]$ for $k_y^b = 40\text{m}^{-1}$ (plots (a) to (c)), $k_y^b = 61.7\ \text{m}^{-1}$ (plots (d) to (f)), $k_y^b = 76\ \text{m}^{-1}$ (plots (g) to (i)) and $k_y^b = 90\ \text{m}^{-1}$ (plots (j) to (l)). Each plot shows a displacement in metres against its corresponding x-coordinate, also in metres. Plots (c), (f), (i) and (l) show the bending mode $\hat{w}$ which exhibits transmission in plot (c), anti-resonance in plot (f), mixed reflection and transmission for the threshold region in plot (i) and reflection in plot (l). The remaining plots show the in-plane wave solution, which remains confined inside the cylindrical region in all cases. Solid and dashed lines show the real and imaginary parts, respectively.

of reflection ($k_y^b = 90\text{m}^{-1}$) and transmission ($k_y^b = 40\text{m}^{-1}$) the expected behaviour is observed. That is, for the reflective case the bending wave function $\hat{w}(x)$ localises to the left as shown in plot (l) of Fig. 7. In the ray tracing model one can pinpoint an exact reflection point, but for the wave problem one observes a decay in amplitude as the wave enters the cylindrical region rather than a hard wall reflection.

In the case of transmission shown in plot (c) of Fig. 7, the bending wave continues through the ridge without significant deformation from the shape of the initial plane wave excitation. This is equivalent to the corresponding ray tracing result. However, if k_y^b is chosen coincide with one of the anti-resonance peaks in the transmission region that were not present in the ray tracing result, then the bending wave field is localised in the central cylindrical region; for example, at $k_y^b = 61.7\text{m}^{-1}$ as shown in plot (f) of Fig. 7. The bending wave function $\hat{w}(x)$ also localises in the cylindrical region when k_y^b is chosen in the threshold region as shown in plot (i) of Fig. 7, which shows a plot of $\hat{w}(x)$ at $k_y^b = 76\ \text{m}^{-1}$.

6. Conclusions

We have investigated bending wave scattering across a smoothed plate and quarter cylinder configuration in the interesting mid-frequency case, close to the ring frequency for the cylinder. Results have been obtained in a simplified and effectively one-dimensional setting using both a high-frequency ray-tracing approximation and a finite difference discretisation of the equivalent full-wave problem. Previous studies on plate and cylinder connections have concentrated on joints having discontinuous curvature where reflections can occur, however the smoothed joints considered here also give rise to reflections within the cylindrical part of the structure. Furthermore, the ray tracing calculations suggest the existence of a threshold incident wave direction which separates waves or rays that exhibit reflective or transmissive behaviour. This threshold direction is also evident from the smoothed transition between reflection and transmission observed in the full wave calculations. Hence, relatively simple scattering laws can be employed to model the propagation of structure-borne noise in shells, and ultimately in built-up structures containing thin shell components. The full wave solution shows that in addition to the switch from transmission to reflection as the incident wave direction becomes increasingly oblique, there are also anti-resonances giving rise to perfect reflection at a discrete set of directions where transmission would typically be expected. In these cases the wave functions appear as trapped modes that localise in the cylindrical part of the configuration.

There are several avenues for further research, including extensions to multiply-curved and fluid-loaded shells. In addition, the scattering laws could be incorporated within computed aided engineering simulations of built-up structures via wave methods, such as the wave and finite element method or dynamical energy analysis.

Acknowledgements

Support from the EU (FP7-PEOPLE-2013-IAPP grant no. 612237(MHiVec)) is gratefully acknowledged. We also wish to thank Dr Gregor Tanner for stimulating discussions and Dr Jonathan Crofts for carefully reading the manuscript.

Appendix A. Tensors and differential geometry

Several physical theories are concisely written in tensor form [19]. The tensor formalism has also proved to be useful in continuum mechanics. The components of tensors are with respect to a given choice of coordinates (x^i). A change of coordinates from (x^i) to $(\tilde{x}^i)$ leads to expressions for components in the new coordinates in relation to those of the old. For example, given a tensor of type $(1,2)$ (that is, with one superscript and two subscript indices) the transformation takes the form

$$\tilde{T}^c_{ab} = \frac{\partial \tilde{x}^c}{\partial x^{c'}} \frac{\partial x^{a'}}{\partial \tilde{x}^a} \frac{\partial x^{b'}}{\partial \tilde{x}^b} T^{c'}_{a'b'} \tag{A.1}$$

where Jacobians and inverse Jacobians have been used for the change of coordinates. We have adopted the important summation convention for repeated indices; this indicates that a summation is to take place over the repeated index (unless otherwise stated).

The metric tensor $g_{\alpha\beta}$, known as the first fundamental form, measures distances via

$$\mathrm{d}s^2 = g_{\alpha\beta}\mathrm{d}x^\alpha \mathrm{d}x^\beta. \tag{A.2}$$

The inverse of the metric tensor $g^{\alpha\beta}$ obeys

$$\delta^\beta_\alpha = g_{\alpha\gamma}g^{\gamma\beta} \tag{A.3}$$

and is used to alter the type of a tensor. For example, we can introduce a new tensor of type (1,1)

$$T^\gamma_\alpha = T_{\alpha\beta}g^{\beta\gamma} \tag{A.4}$$

from a tensor of type (0,2) by raising the indices of the latter tensor. Likewise $g_{\alpha\beta}$ lowers indices.

The directional derivative in arbitrary coordinates is generalized to the covariant derivative D_α. This derivative may be introduced from an embedding using projection of gradients [10,23] or intrinsically with quantities only related to the curved space itself [24]. For example, in a coordinate basis, the covariant derivative of a tensor of type (1,1) becomes

$$D_\alpha u^\epsilon_\beta = \partial_\alpha u^\epsilon_\beta - \Gamma^\gamma_{\alpha\beta}u^\epsilon_\gamma + \Gamma^\epsilon_{\alpha\gamma}u^\gamma_\beta \tag{A.5}$$

with

$$\Gamma^i_{kl} = \frac{1}{2}g^m\left(\partial_l g_{mk} + \partial_k g_{ml} - \partial_m g_{kl}\right) \tag{A.6}$$

the Christoffel symbols.

Appendix B. Parameter values for the numerical studies

The computations throughout this work were done using the following parameter choices [8,21]:

- $R = 0.055$ m
- $h = 5.3 \times 10^{-4}$ m
- $x^* = 0.0432$ m
- $\delta x = 0.0144$ m
- $E = 1.95 \times 10^{11}$ Pa
- $\rho = 7700\ \mathrm{kg/m^3}$
- $\nu = 0.28$
- $\omega = 9742\pi$ Rad/s

References

[1] O.C. Zienkiewicz, R.L. Taylor, J.Z. Zhu, *The Finite Element Method: Its Basis and Fundamentals*, 7th edition, Butterworth-Heinemann, Oxford, 2003.

[2] R.H. Lyon, R.G. DeJong, *Theory and Application of Statistical Energy Analysis*, 2nd edition, Butterworth-Heinemann, Boston MA, 1995.

[3] A.S. Glasser, *An Introduction to Ray Tracing*, Academic Press, New York, 1989.

[4] A. Le Bot, *Foundation of Statistical Energy Analysis in Vibroacoustics*, Oxford University Press, Oxford, 2015.

[5] H. Kuttruff, Room Acoustics, 4th edition, Spon, London, 2000.

[6] V. Cerveny, *Seismic Ray Theory*, Cambridge University Press, Cambridge UK, 2001.

[7] A.N. Norris, D.A. Rebinsky, Membrane and flexural waves on thin shells, *Journal of Vibration and Acoustics* 116 (1994) 457–467, http://dx.doi.org/10.1115/1.2930449.

[8] E.G. Williams, B.H. Houston, J.A. Bucaro, Experimental investigation of the wave propagation on a point-driven, submerged capped cylinder using K-space analysis, *Journal of the Acoustical Society of America* 87 (2) (1990) 513–522, http://dx.doi.org/10.1121/1.398922.

[9] R.S. Langley, Wave motion and energy flow in cylindrical shells, *Journal of Sound and Vibration* 169 (1) (1994) 29–42, http://dx.doi.org/10.1006/jsvi.1994.1004.

[10] A.N. Norris, Reflection and transmission of structural waves at an interface between doubly curved shells, *Acta Acustica united with Acustica* 84 (6) (1998) 1066–1076.

[11] G. Tanner, Dynamical energy analysis - Determining wave energy distributions in vibro-acoustical structures in the high-frequency regime, *Journal of Sound and Vibration* 320 (2009) 1023–1038, http://dx.doi.org/10.1016/j.jsv.2008.08.032.

[12] D.J. Chappell, D. Löchel, N. Søndergaard, G. Tanner, Dynamical energy analysis on mesh grids: *a new tool for describing the vibro-acoustic response of engineering structures*, *Wave Motion* 51 (4) (2014) 589–597, http://dx.doi.org/10.1016/j.wavemoti.2014.01.004.

[13] E. Manconi, B.R. Mace, Wave characterization of cylindrical and curved panels using a finite element method, *Journal of the Acoustical Society of America* 125 (1) (2009) 154–163, http://dx.doi.org/10.1121/1.3021418.

[14] J.M. Renno, B.R. Mace, Calculation of reflection and transmission coefficients of joints using a hybrid finite element/wave and finite element approach, *Journal of Sound and Vibration* 332 (9) (2013) 2149–2164, http://dx.doi.org/10.1016/j.jsv.2012.04.029.

[15] J.T. Kayija, The rendering equation, *ACM SIGGRAPH Computer Graphics* 20 (4) (1986) 143–150, http://dx.doi.org/10.1145/15886.15902.

[16] P. Gaspard., *Chaos, Scattering and Statistical Mechanics*, Cambridge University Press, Cambridge UK, 1998.

[17] P. Cvitanović, R. Artuso, R. Mainieri, G. Tanner, G. Vattay Chaos: Classical and Quantum , `ChaosBook.org`, Niels Bohr Institute, Copenhagen, Denmark, 2012.

[18] A.D. Pierce, Waves on fluid-loaded inhomogeneous elastic shells of arbitrary shape, *Journal of Vibration and Acoustics* 115 (4) (1993) 384–390, http://dx.doi.org/10.1115/1.2930361.

[19] W. Flügge, *Tensor Analysis and Continuum Mechanics*, Springer, Berlin, 1972.

[20] C.F. Van Loan, The ubiquitous Kronecker product, *Journal of Computational and Applied Mathematics* 123 (2000) 85–100, http://dx.doi.org/10.1016/S0377–0427(00)00393–9.

[21] D.A. Rebinsky, A.N. Norris, Dispersion of flexural waves on shells, *Journal of Vibration and Acoustics* 118 (3) (1996) 526–529, http://dx.doi.org/10.1115/1.2888218.

[22] N. Søndergaard, D.J. Chappell, G. Tanner, Tracking vibrational energy on curved shell structures in the mid-high frequency limit - a ray-tracing approach. Proceedings of Noise and Vibration - Emerging Technologies (NOVEM) 2015, Dubrovnik, Croatia, 2015.

[23] M. do Carmo, *Differential geometry of curves and surfaces*, Prentice Hall, New Jersey, 1976.

[24] T. Frankel, *The Geometry of Physics*, Cambridge University Press, New York, 2004.